Zinc(II) and copper(II) complexes with benzothiadiazole Schiff-base ligands †

Nataliya Plyuta, Thomas Cauchy, Andreas Hauser, Francesc Lloret, Miguel Julve, Narcis Avarvari

Zinc(II) and copper(II) complexes with benzothiadiazole Schiff-base ligands[†]

Nataliya Plyuta,[a,b] Thomas Cauchy,[a,*] Andreas Hauser,[c] Francesc Lloret,[d] Miguel Julve,[d] Narcis Avarvari[a,*]

[a] *Univ Angers, CNRS, MOLTECH-Anjou, SFR MATRIX, F-49000 Angers, France. E-mail: thomas.cauchy@univ-angers.fr; narcis.avarvari@univ-angers.fr*

[b] *Department of Inorganic Chemistry, Taras Shevchenko National University of Kyiv, Volodymyrska str. 64/13, Kyiv 01601, Ukraine*

[c] *Department of Physical Chemistry, University of Geneva, 30 Quai Ernest-Ansermet, 1211 Geneva, Switzerland*

[d] *Instituto de Ciencia Molecular (ICMol)/Departament de Química Inorgànica, Universitat de València, C/ Catedrático José Beltrán 2, 46980 Paterna (València), Spain*

[†] *Dedicated to Professor Ionel Haiduc on the occasion of his 85th birthday*

Abstract

The ligand (2-[4-(2,1,3-benzothiadiazole)imino]methyl-phenol) HL^1 containing the electron poor benzothiadiazole (BTD) unit, conveniently prepared by condensation of 4-amino-2,1,3-benzothiadiazole and salicylaldehyde, has been structurally characterized by single crystal X-ray diffraction. Two energy minima have been determined, by DFT calculations, for HL^1 and for its *ortho*-vanillin analogue HL^2, corresponding either to the conformer observed in the solid state or to the chelating tridentate form. TD-DFT calculations have been performed on HL^1 and HL^2 in order to assign their experimental UV-visible absorption bands. Reaction of HL^1 and HL^2 with copper (II) hexafluoroacetylacetonate (hfac), zinc (II) hexafluoroacetylacetonate or zinc (II) acetate provided the neutral complexes $[Cu(L^1)(hfac)]$ (**1**), $[Zn(L^1)_2]$ (**2**), $[Cu(L^2)_2]$ (**3**) and $[Zn(L^2)_2]$ (**4**) which were structurally characterized, with a focus on the coordination sphere of the metal centre and on the intermolecular interactions. The UV-visible absorption properties of the Zn(II) complexes **2** and **4** have been experimentally and theoretically investigated and compared to those of the ligands. Finally, the cryomagnetic study of **1** and **3** in the temperature range 2.0 – 295.0 K reveals a Curie-Weiss law behaviour with very weak intermolecular antiferromagnetic interactions in the low temperature region.

Keywords

Benzothiadiazole; Schiff-base ligands; Crystal structures; Zinc complexes; Copper complexes

1. Introduction

The association of coordinating groups with the 2,1,3-benzothiadiazole (BTD) unit [1,2], extensively used in the structure of molecular precursors or polymers for organic electronics [3,4,5,6,7,8] and also in redox switchable donor-acceptor systems [9,10], finds interest in the access to functional ligands and derived complexes [11]. For example, BTD-dicarboxylate systems provided luminescent coordination polymers [12,13,14,15], while dipyridyl-BTD derivatives [16,17] show excellent luminescent properties which persist in Zn(II) or Ag(I) complexes and coordination polymers [18,19]. Schiff-base ligands obtained from the condensation of either 5,6-diamino-BTD [20] or 4-amino-BTD [21,22] with carbonyl compounds have been also described together with their Zn(II) [20,22] or Cu(I) [21] complexes. In this respect, particularly interesting carbonyl precursors providing chelating Schiff-base units are salicylaldehyde and *ortho*-vanillin [23,24,25]. For example, the salicylaldehyde derivative 4-(hexyloxy)-2-hydroxybenzaldehyde was condensed with 5,6-diamino-BTD to provide the BTD-salen I (Chart 1) which was used as chelating agent for Zn(II) [20]. However, the N_{BTD} atoms in this ligand do not participate to the coordination sphere of the metal centre. We have very recently reported the condensation of 4-amino-BTD with *ortho*-vanillin which afforded a BTD-*ortho*-vanillin Schiff-base ligand (HL^2 in Chart 1). The proximity of the thiadiazole and *ortho*-vanillin units in this new ligand creates a favourable environment for a tris-chelation involving the adjacent BTD nitrogen atom. We have shown that its neutral cobalt(II) complex of formula $[Co(L^2)_2]\cdot CH_2Cl_2$, where the two deprotonated monoanionic ligands chelate the metal centre within a *NNO* tridentate mode, behaves as a field-induced single-molecule magnet (SMM) [26].

As a continuation of our research line devoted to functional BTD ligands and complexes, we report herein the synthesis, crystal structure and DFT and TD-DFT calculations of the new BTD Schiff-base ligand (2-[4-(2,1,3-benzothiadiazole)imino]methyl-phenol), hereafter noted HL^1 (Chart 1). Its coordination ability and that of the previously described BTD-*ortho*-vanillin ligand HL^2 with Cu(II) and Zn(II) is investigated and the resulting mononuclear complexes are structurally characterized and included herein together with the UV-Vis absorption properties of the Zn(II) complexes, supported by TD-DFT calculations, and the cryomagnetic study of the Cu(II) complexes.

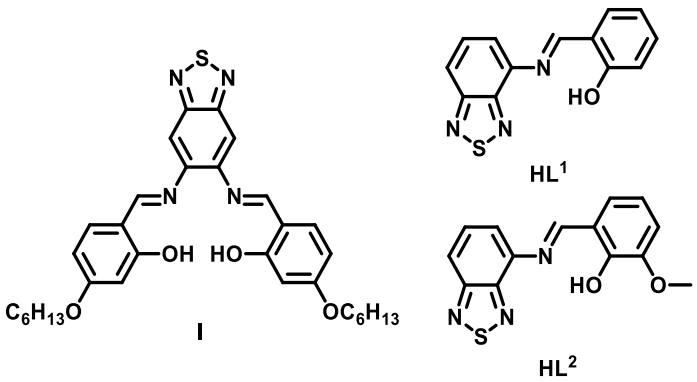

Chart 1. BTD Schiff-base ligands. HL^1 and HL^2 are investigated in this work.

2. Experimental

2.1 General considerations

Starting chemicals were purchased from commercial sources and used as received. All the reactions were carried out under ambient conditions with HPLC-grade solvents. Nuclear magnetic resonance spectra were recorded on a Bruker Avance DRX 300 spectrometer operating at 300 and 75 MHz for ^{1}H and ^{13}C, respectively. Chemical shifts are expressed in parts per million (ppm) downfield from external TMS. The following abbreviations (δ) are used: s, singlet; d, doublet; t, triplet; m, multiplet. MALDI-TOF MS spectra were done on a Bruker Biflex-IIITM apparatus, equipped with a 337 nm N_2 laser. ESI-MS spectra were achieved on a Bruker MicrO-Tof-Q 2 spectrometer. Elemental analyses (C, H, N and S) were recorded using a Flash 2000 Fisher Scientific Thermo Electron analyzer. The IR spectra were recorded using PerkinElmer Spectrum BX spectrometer for the samples pressed into pellets of KBr or ATR Bruker Vertex 70 spectrophotometer in the range 4000-400 cm^{-1} (at 1 cm^{-1} resolution). Signal intensities (height) are denoted by the following abbreviations: vs-very strong, s-strong, m-medium and w-weak. UV-Vis absorption spectra of the ligands in methylene chloride at concentrations of around 0.05 mM and of the complexes in DMSO at concentrations of around 0.2 mM were measured on a Cary 5000 (Agilent) spectrophotometer. Steady-state emission and excitation spectra likewise were recorded on a Fluorolog 3 (Horiba-Jobin-Yvon) spectrophotometer and corrected for the spectral response of the apparatus.

2.2. Synthesis

Synthesis of 4-amino-2,1,3-benzothiadiazole and ligand HL^2 were performed according to the previously reported procedure (Fig. S1 for the ^{1}H NMR spectra in DMSO-d^6) [26].

2.2.1. Synthesis of the ligand 2-[4-(2,1,3-benzothiadiazole)imino]methyl-phenol (HL^1)

4-Amino-2,1,3-benzothiadiazole (5 g, 33.07 mmol) and salicylaldehyde (3.53 ml, 33.07 mmol) were dissolved in ethanol (40 ml), forming a yellow-orange solution, which was magnetically stirred at 80 °C for 4 h. The yellow-orange solid was filtered and dried in air. Yield: 6.31 g (75%). ^{1}H RMN

(300 MHz, $CDCl_3$) δ 13.38 (s, 1H), 9.51 (s, 1H), 7.92 (d, *J* = 8.8 Hz, 1H), 7.70 – 7.63 (m, 1H), 7.53 – 7.39 (m, 3H), 7.07 (d, *J* = 8.4 Hz, 1H), 6.98 (t, *J* = 7.5 Hz, 1H) (Fig. S2). ^{1}H NMR (500 MHz, DMSO-d^6) δ 13.03 (s, 1H), 9.39 (d, J = 4.9 Hz, 1H), 8.02 (dd, J = 8.8, 0.9 Hz, 1H), 7.81 (dd, J = 8.8, 7.2 Hz, 1H), 7.75 (dd, J = 7.9, 1.7 Hz, 1H), 7.68 (dd, J = 7.2, 3.7 Hz, 1H), 7.50 – 7.46 (m, 1H), 7.05 – 7.01 (m, 2H) (Fig. S3). ^{13}C RMN (76 MHz, $CDCl_3$) δ 166.31, 161.31, 155.95, 149.52, 133.52, 132.64, 129.57, 121.17, 119.48, 119.18, 118.96, 117.21 (Fig. S4). IR (ATR, ν_{max} cm^{-1}): 3072w, 1606s, 1568s, 1523s, 1479s, 1455s, 1411m, 1319s, 1284s, 1201s, 1152s, 1116s, 1071s, 1030m, 980m, 914s, 853s, 837s, 810vs, 760vs, 747vs, 667s, 616m, 597m, 550m, 522m, 504s, 471m, 454m, 445s. Exact mass, m/z 255.0459. Anal. Calcd for $C_{13}H_9N_3OS$ (%): C, 61.16; H, 3.55; S, 12.56; N, 16.46. Found (%): C, 60.82; H, 3.57; S, 12.38; N, 16.47.

*2.2.2. Synthesis of [Cu(L^1)(hfac)] (**1**)*

A solution of copper(II) hexafluoroacetylacetonate hydrate (37 mg, 0.078 mmol) in methanol (3 mL) was added to a yellow solution of HL^1 (20 mg, 0.078 mmol) in methylene chloride (3 mL). The reaction mixture was magnetically stirred at 65 °C for 2 hours. After 1-3 days of slow evaporation, red needle-shaped crystals were collected by filtration. Yield: 26 mg (53 %). IR (KBr, ν_{max} cm^{-1}): 3442br, 2938m, 1650s, 1610vs, 1584s, 1524vs, 1483s, 1431s, 1389m, 1321w, 1261vs, 1204vs, 1150vs, 909w, 808w, 751m, 740w, 655w, 448w, 425w. MALDI-TOF MS (m/z): 317.0 $[CuL^1]^+$.

*2.2.3. Synthesis of $Zn(L^1)_2$ (**2**)*

A solution of zinc(II) hexafluoroacetylacetonate dihydrate (20 mg, 0.039 mmol) in methanol (3 mL) was added to a yellow solution of HL^1 (20 mg, 0.078 mmol) in methylene chloride (3 mL). The reaction mixture was magnetically stirred at 65 °C for 2 hours. After 1-3 days of slow evaporation, prismatic yellow crystals were collected by filtration. Yield: 7 mg (31 %). ^{1}H NMR (500 MHz, DMSO-d^6) δ 8.99 (s, 2H), 7.81 (d, J = 9.1 Hz, 1H), 7.69 – 7.64 (m, 1H), 7.61 (d, J = 6.8 Hz, 1H), 7.46 (d, J = 6.2 Hz, 1H), 7.27 (t, J = 7.7 Hz, 1H), 6.57 (t, J = 6.9 Hz, 1H), 6.49 (d, J = 8.3 Hz, 1H) (Fig. S5). IR (KBr, ν_{max} cm^{-1}): 3332br, 1610vs, 1528s, 1500s, 1456s, 1440s, 1410w, 1390w, 1340w, 1280s, 1200s, 1148s, 1092w, 1070w, 1028w, 978w, 904m, 888m, 848m, 808m, 758vs, 654w, 522w, 452w. ESI-MS (m/z): 317.9 $[ZnL^1]^+$, 572.97 $[Zn(L^1)_2]$.

*2.2.4. Synthesis of $Cu(L^2)_2$ (**3**)*

A solution of copper(II) hexafluoroacetylacetonate hydrate (17 mg, 0.035 mmol) in methanol (3 mL) was added to a red-orange solution of HL^2 (20 mg, 0.070 mmol) in methylene chloride (3 mL). The reaction mixture was magnetically stirred at 65 °C for 2 hours. After 1-3 days of slow evaporation, prismatic red crystals were collected by filtration. Yield: 15 mg (68 %). IR (KBr, ν_{max}

cm^{-1}): 3449br, 2938m, 1605vs, 1544m, 1530s, 1466s, 1446s, 1390m, 1340w, 1244vs, 1210vs, 1082m, 1066w, 986w, 904w, 824w, 742m, 502w. MALDI-TOF MS (m/z): 347.0 $[CuL^2]^+$, 654.0 $\{Na[Cu(L^6)_2]\}^+$.

*2.2.5. Synthesis of $Zn(L^2)_2$ (**4**)*

A solution of zinc(II) acetate dihydrate (8 mg, 0.035 mmol) in methanol (3 mL) was added to a red-orange solution of HL^2 (20 mg, 0.070 mmol) and triethylamine (0.01 mL, 0.070 mmol) in methylene chloride (3 mL). The reaction mixture was magnetically stirred at 65 °C for 2 hours. After 1-3 days of slow evaporation, prismatic yellow-orange crystals were collected by filtration. Yield: 9 mg (44 %). ^{1}H NMR (500 MHz, DMSO-d^6) δ 8.95 (s, 1H), 7.77 (d, J = 8.7 Hz, 1H), 7.66 – 7.61 (m, 1H), 7.55 (d, J = 7.3 Hz, 1H), 7.07 (d, J = 6.8 Hz, 1H), 6.91 – 6.85 (m, 1H), 6.49 (t, J = 7.8 Hz, 1H), 3.57 (s, 3H) (Fig. S6). IR (ATR, ν_{max} cm^{-1}): 1739m, 1696m, 1643m, 1606s, 1532m, 1486m, 1435s, 1368s, 1255s, 1203vs, 1142vs, 1094m, 967m, 903m, 849m, 800s, 735s, 665s, 585m, 527m, 492s, 445m, 421m. MALDI-TOF MS: 655.0 $\{Na[Zn(L^2)_2]\}^+$.

2.3. Crystal structure determinations

Single crystals of the compounds were mounted on glass fibre loops using a viscous hydrocarbon oil to coat the crystal and then transferred directly to a cold nitrogen stream for data collection. Data collections were mostly performed at 150 K on an Agilent Technologies SuperNova diffractometer equipped with an Atlas CCD detector and micro-focus Cu-Kα radiation (λ = 1.54184Å). The structures were solved by direct methods SHELXS-97 [27] and refined on F^2 by full matrix least-squares techniques using the SHELX97 program [28] within WINGX [29]. All non-H atoms were refined anisotropically and multiscan empirical absorption was applied using the CrysAlisPro program (CrysAlisPro, AgilentTechnologies, V1.171.38.41r, 2015). The hydrogen atoms were introduced at calculated positions (riding model) and included in structure factor calculations but not refined. Details about data collection and solution refinement are given in Table 1. Supplementary crystallographic Figs. S7-S13 and Tables S1-S9 are reported in the ESI.

Crystallographic data for the five structures have been deposited with the Cambridge Crystallographic Data Centre, deposition numbers CCDC 2167426 (HL^1), CCDC 2167427 (**1**), CCDC 2167428 (**2**), CCDC 2167429 (**3**), and CCDC 2167430 (**4**). These data can be obtained free of charge from CCDC, 12 Union road, Cambridge CB2 1EZ, UK (e-mail: deposit@ccdc.cam.ac.uk or http://www.ccdc.cam.ac.uk).

Table 1. Crystallographic data, details of data collection and structure refinement parameters for HL^1 and **1**-**4**

	HL^1	$[Cu(L^1)(hfac)]$ (**1**)	$[Zn(L^1)_2]$ (**2**)	$[Cu(L^2)_2]$ (**3**)	$[Zn(L^2)_2]$ (**4**)

Formula	$C_{13}H_9N_3OS$	$C_{18}H_9CuF_6N_3O_3S$	$C_{26}H_{16}N_6O_2S_2Zn$	$C_{28}H_{20}CuN_6O_4S_2$	$C_{28}H_{20}N_6O_4S_2Zn$
M ($g \cdot mol^{-1}$)	255.29	524.88	573.94	632.16	633.99
T (K)	150.00(10)	294.21(10)	150.00(10)	150.00(10)	149.3(4)
Wavelength (Å)	1.54184	1.54184	1.54184	1.54184	1.54184
Crystal system	Orthorhombic	Monoclinic	Orthorhombic	Monoclinic	Monoclinic
Space group	*P*bca	$P2_1/c$	*P*bcn	$P2_1/c$	$P2_1/c$
a, (Å)	12.9117(3)	8.3214(2)	19.8956(10)	7.2857(2)	14.2736(3)
b, (Å)	9.3341(2)	21.7762(4)	8.3892(4)	22.5527(5)	8.39650(10)
c, (Å)	18.8634(5)	10.5087(2)	13.8731(7)	7.8865(2)	21.6214(4)
α, (°)	90	90	90	90	90
β, (°)	90	93.263(2)	90	98.126(2)	99.887(2)
γ, (°)	90	90	90	90	90
V, $Å^3$	2273.40(9)	1901.18(7)	2315.5(2)	1282.84(6)	2552.80(8)
Z, $\rho_{calcd.}$ (g/cm^3)	8, 1.492	4, 1.834	4, 1.646	2, 1.637	4, 1.650
μ (mm^{-1})	2.452	3.468	3.494	3.148	3.293
F (000)	1056	1044	1168	646	1296
R_{int}	0.0215	0.0176	0.0340	0.0203	0.0712
R_1 [I>2σ(I)]	0.0338, 0.0916	0.0446, 0.1212	0.0354, 0.0925	0.0383, 0.1115	0.0719, 0.1950
wR_2 (all data)	0.0378, 0.0950	0.0515, 0.1272	0.0451, 0.1011	0.0423, 0.1147	0.0739, 0.1995
G.O.F.	1.056	1.056	1.040	1.058	1.059
№ CCDC	2167426	2167427	2167428	2167429	2167430

2.4 Computational details

Theoretical calculations have been performed using the Gaussian 09 package [30], with the PBE0 hybrid functional [31] (with 25% of exact exchange) and TZVP basis set from Ahlrichs and coworkers [32,33]. Optimized geometries were then confirmed as global minima by frequency calculations. Starting geometry for *A*-HL^{1-2}, compounds **2** and **4** were derived from the X-ray structure. Hirshfeld population analysis including interatomic electrostatic interactions has been used [34,35]. For the calculations of the excited states, a Time Dependent DFT methodology has been employed with the same parameters as for the ground states. The pictures of the molecular orbitals, molecular electrostatic potentials and electron density difference plots (between ground and excited state) have been generated by quchemreport, a homemade python program based on cclib that automate the quality control and report generation [36,37]. More details and supplementary theoretical Figs. S14-S61 and Tables S10-S39 are reported in the ESI.

2.5 Magnetic measurements

Variable-temperature (2.0 – 295 K) magnetic susceptibility measurements on polycrystalline samples of **1** and **3** were carried out with a SQUID magnetometer. The experimental data were corrected for the diamagnetic contribution of the constituent atoms, estimated as -220 x 10^{-6} (**1**) and -556 x 10^{-6} cm^3 mol^{-1} (**3**), and the sample holder, as well as for the temperature-independent paramagnetism (TIP) of the copper(II) ion (60 x 10^{-6} cm^3 mol^{-1}).

3. Results and discussion

3.1. General synthetic strategy

The BTD Schiff-base ligand HL^1 was obtained in a good yield as a yellow-orange precipitate by the condensation of 4-amino-2,1,3-benzothiadiazole with salicyl aldehyde in ethanol (Scheme 1). The synthetic procedures of 4-amino-2,1,3-benzothiadiazole and HL^2 have been optimized previously [26].

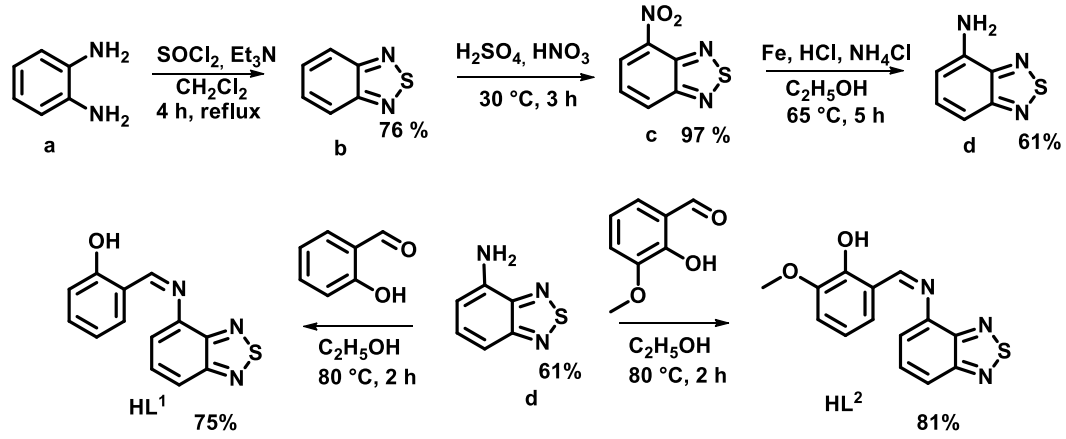

Scheme 1. Synthesis of the BTD Schiff-base ligands HL^1 and HL^2.

To study the coordination ability of the BTD Schiff base ligands, we used as metal precursor zinc(II) and copper(II) hexafluoroacetylacetonates. The ligand HL^1 was reacted with $Cu(hfac)_2 \cdot H_2O$ in a mixture of methanol and methylene chloride (1:1 *v/v*) to form the complex $[Cu(L^1)(hfac)]$ (**1**), regardless of the ratio of the starting materials. In the case of $Zn(hfac)_2 \cdot 2H_2O$ we obtained the neutral complex $[Zn(L^1)_2]$ (**2**). The complex $[Cu(L^2)_2]$ (**3**) was synthesized similarly as complex **1** by using HL^2. Using $Zn(hfac)_2 \cdot 2H_2O$ with HL^2 proved to be unsuccessful to isolate a crystalline complex. Therefore, we used the same approach as for the synthesis of the complex $[Co(L^2)_2] \cdot CH_2Cl_2$ [26]. The complex $[Zn(L^2)_2]$ (**4**) was thus obtained from HL^2 and zinc acetate in the presence of triethylamine.

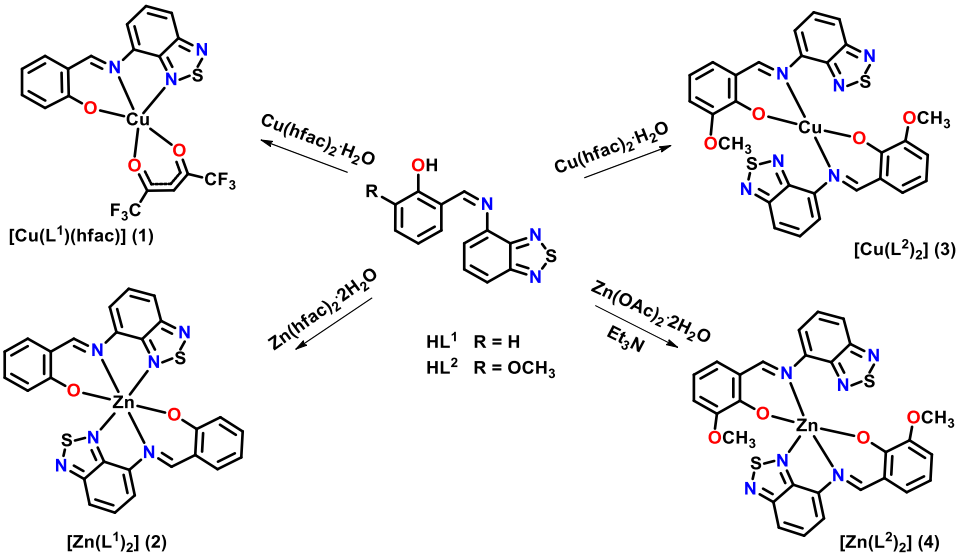

Scheme 2. Synthesis of complexes **1-4**.

3.2. Crystal structure of HL[1] and DFT calculations on HL[1] and HL[2]

Suitable single crystals of the ligand HL^1 for X-ray analysis have been obtained upon slow evaporation of a methanol/ methylene chloride (1:1 v/v) solution. HL^1 crystallized in the centrosymmetric orthorhombic *P*bcn space group. The structure is not fully planar and shows an intramolecular hydrogen bond between the OH group and the N atom of the imino group (Fig.1, Table 2). The torsion angle C(7)-N(3)-C(6)-C(1) between the BTD and phenyl ring is 26.9°. As shown in Fig.1 and Table 2, there are weak intermolecular C-H···N interactions between two adjacent molecules in the crystal structure (see also Fig. S7).

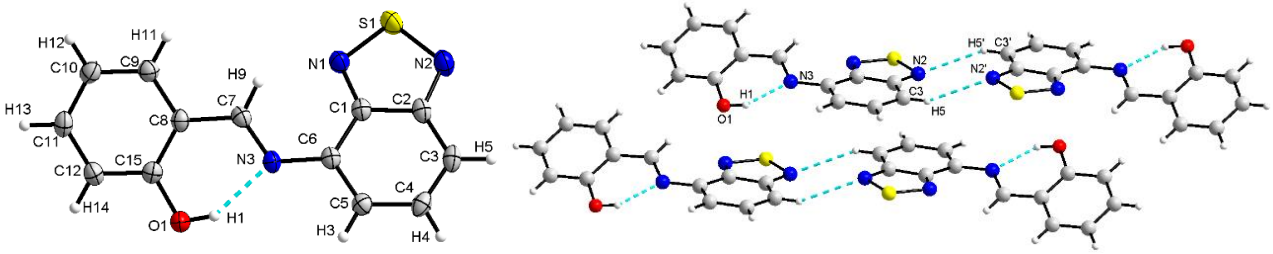

Fig. 1. ORTEP diagram of the crystal structure of HL^1, with displacement ellipsoids drawn at the 50% probability level (left) and fragment of the crystal structure with H-bond interactions (right).

Table 2. Hydrogen bonds parameters (Å, °) for HL^1.

A···H – D	d(A···H), Å	d(A···D) , Å	∠ (D – H···A), °
N(3) ···H(1) – O(1)	1.889	2.615	146.89
N(2) ···H(5)^{I} – C(3)^{I}	2.618	3.473	153.09

Symmetry code: (i) -x,2-y,-1-z.

Next, we have performed DFT calculations on both HL^1 and HL^2 molecules in order to compare the experimental conformations with the optimized ones in the gas phase. The starting geometries for HL^1 and HL^2 were derived from their X-ray structures [26]. Upon optimization, it can be observed

that the experimental geometry is in good agreement with the calculated bond lengths and angles of the *A*-conformer of the ligands, where the thiadiazole ring is *anti* with respect to the OH group (Fig. 2).

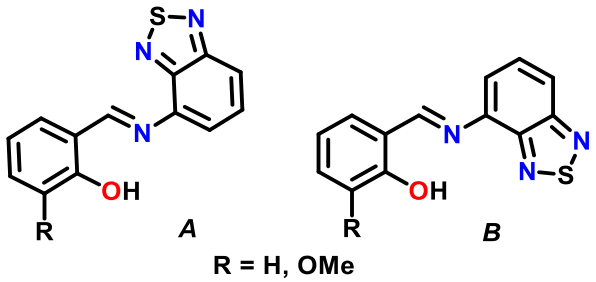

Fig. 2. *A*- and *B*-conformers for HL^1 (R = H) and HL^2 (R = OMe).

A slight deviation from planarity between the salicylidene and BTD moieties was observed. In the calculated geometry, the C(7)N(3)C(6)C(1) dihedral angle is equal to 2.93 (HL^1) and 0° (HL^2) (atom numbering in Fig. 1). The starting geometries for the *B*-conformers of the Schiff-bases were manually generated by changing the dihedral angle. In the resulting optimized *B*-conformers the C(7)N(3)C(6)C(1) dihedral angle is equal to 143.81 for HL^1 and 142.64° for HL^2, respectively. Calculations show that the *A*-conformer of HL^1 and HL^2 is more stable in the gas phase, which was in agreement with the SCXRD analysis. The values of the difference in the Gibbs free energies are 2.7 (HL^1) and 5.3 kcal·mol^{-1} (HL^2).

Furthermore, DFT calculations were performed for the deprotonated molecules in order to estimate their coordination abilities. HOMO and HOMO–1 for the deprotonated ligands L^1 and L^2 are shown in Table 3. It should be noted that the topologies of the molecular orbitals are similar for L^1 and L^2. HOMO and HOMO–1 are mainly located on the phenol ring, oxygen and nitrogen atoms. For the coordination properties of the ligands, we will focus on the *N*- and *O*-donor atoms. The π type HOMO and *n* type HOMO–1 are located on phenolic *O* and imine *N* atoms. The BTD ring does not have any participation in the HOMO and HOMO–1, therefore we can hypothesize that its coordination to metal centres will be much weaker compared to the Schiff-base unit. Considering its symmetry, we can expect as well that HOMO–1 corresponds to the orbital taking part in coordination. Accordingly, the main coordination motif should be defined by the O_{phen} and the N_{Im} atoms. The LUMO's are essentially localized on the benzothiadiazole ring, confirming that this fragment has acceptor properties. Coordination through *N* from BTD is not favoured, the M–N_{BTD} bonds being expected to be weaker, with long M–N distances. The LUMO's topology is in favour of a π back-bonding interaction with the metal atom.

Table 3. LUMO, HOMO and HOMO–1 for L^1 and L^2.

	LUMO	HOMO	HOMO-1
L^1	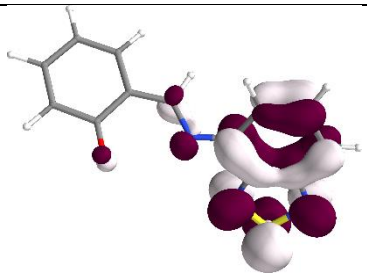	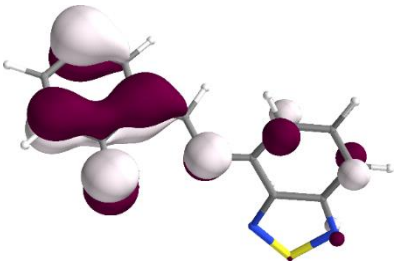	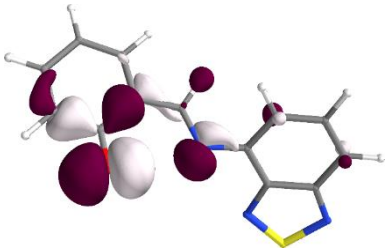
	0.67 eV	-1.68 eV	-2.39 eV
L^2	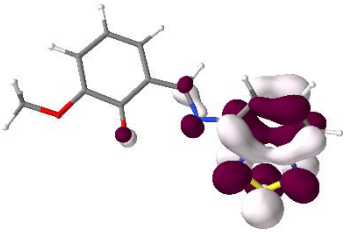	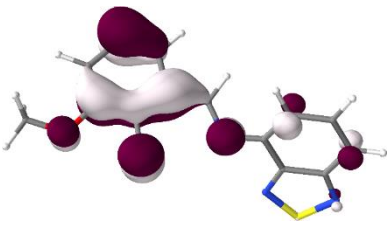	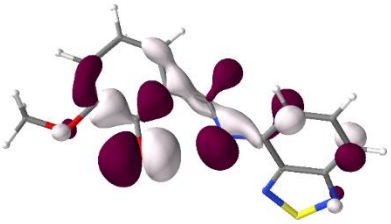
	0.72 eV	-1.54 eV	-2.47 eV

Hirshfeld charges for the oxygen and nitrogen atoms of the deprotonated ligands are reported in Table 4. The greatest negative charges correspond to oxygen of the phenyl group and nitrogen of the imino group. The N_{BTD} atoms have the lowest negative charges. That confirms the electron deficiency of the BTD unit. The molecular electrostatic potential mapped on the electron density at the van der Waals radii for L^1 and L^2 are represented in Fig. 3. The red colour illustrates the most negative potentials (electron-rich regions), while the blue one corresponds to the most positive potentials (electron-poor regions). The most negative potentials can be observed near the O_{Phen} and the N_{Im} atoms and the most positive ones near the S atom of BTD unit.

Table 4. Hirshfeld charges for L^1 and L^2.

	$O(2)_{Me}$	$O(1)_{Phen}$	$N(3)_{Im}$	$N(1)_{BTD}$	$N(2)_{BTD}$
L^1	-	-0.419	-0.378	-0.218	-0.269
L^2	-0.236	-0.395	-0.380	-0.218	-0.270

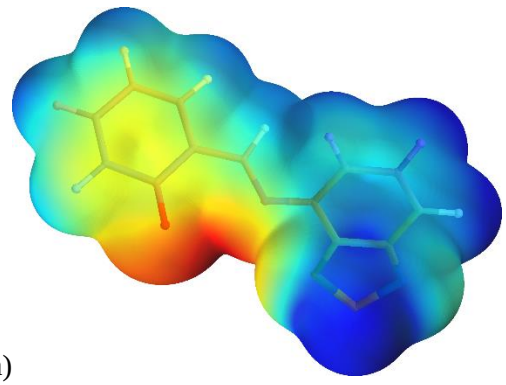

a)

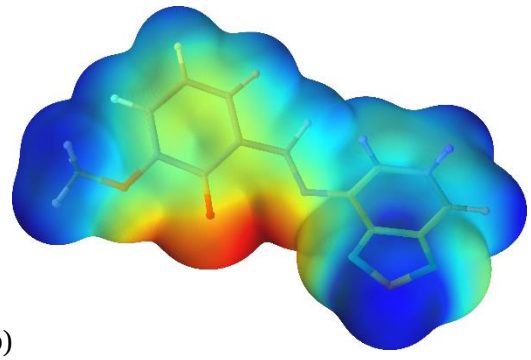

b)

Fig. 3. Representation of the molecular electrostatic potential mapped on the electron density: a) L^1; b) L^2 (cutoff value of 0.002 e^- $bohr^{-3}$). Red, blue and green regions correspond to the most negative potentials, the most positive potentials and intermediate values, respectively.

*3.3. Crystal structures of the complexes **1-4***

Complex **1** crystallizes in the monoclinic $P2_1/c$ space group. The copper ion is coordinated by the deprotonated ligand and a hfac co-ligand (Fig. 4). The coordination environment of Cu(II) is formed by the N_2O_3 motif within a square pyramidal geometry, the deformation from the ideal symmetry being small, $\tau = 0.05$ [38]. Selected bond lengths and angles are given in Table 5. The molecules of the complex form supramolecular chains through π-π stacking: I – between benzothiadiazole fragments [3.552 Å] and II – salicylidene moieties [3.564 Å] of the neighbouring complexes (see also Fig. S8).

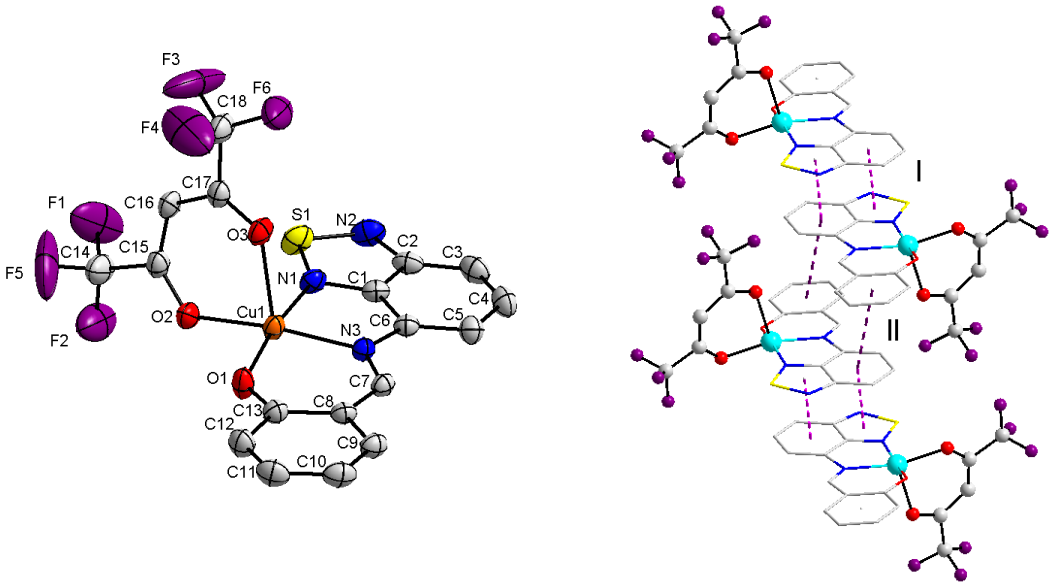

Fig. 4. ORTEP diagram of the crystal structure of **1** showing the atom numbering (left). View of a fragment of the crystal packing of **1** showing the π-π interactions as dashed lines (right).

Complex **2** crystallizes in the centrosymmetric orthorhombic *P*bcn space group, with one crystalographically independent molecule in the unit cell (Fig. 5). The metal ion is coordinated by two ligands L^1 displaying a chelating *O,N,N'*-tridentate coordination mode. The coordination environment of Zn(II) is formed by the donor atoms of the two ligands, that is a N_4O_2 motif. The geometry of the polyhedron is rather distorted; such deformation may be due to the rigid ligand geometry, which ensures a chelating function. The ligands are oriented around the central atom in the *mer*-configuration. The Zn–N_{BTD} bonds are elongated compared to the Zn–N_{Im} ones (Table 5). Moreover, the Zn-N_{BTD} bond distance here is a little elongated compared to other Zn-N_{BTD} distances

reported in the literature; for example, it varies between 2.04 – 2.14 Å for four-coordinated zinc ions [39,40] and between 2.10 – 2.32 Å for hexa-coordinated zinc ions [19,41,42].

SHAPE analysis for the coordination environment $\{N_4O_2\}$ of the zinc(II) ion indicates a distorted octahedron, with a SHAPE analysis value of 2.080 (Table S9 in ESI) [43,44].

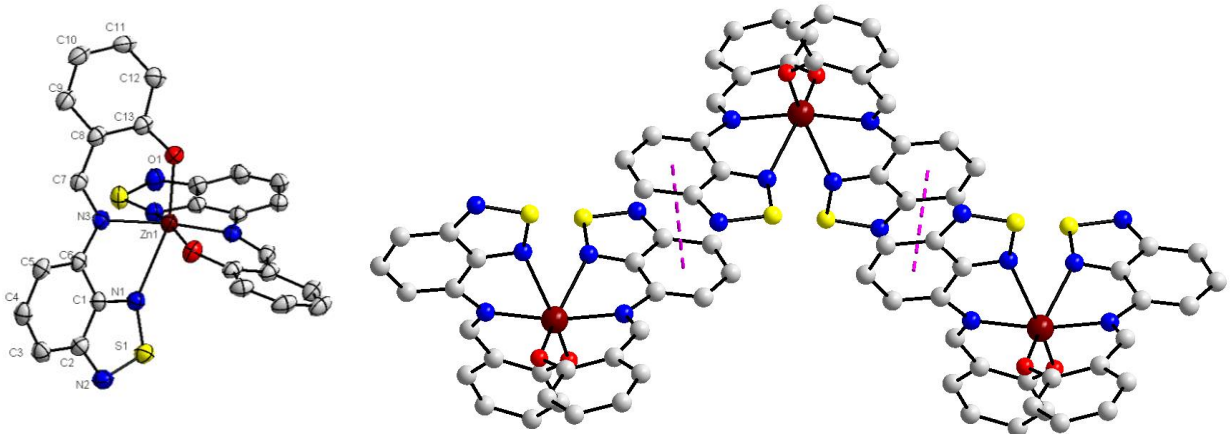

Fig. 5. ORTEP diagram of the crystal structure of complex **2** (left). Fragment of the crystal structure with π-π stacking interactions highlighted (dotted) (right).

Table 5. Selected geometrical parameters for complexes **1**-**4**.

	[Cu(L^1)(hfac)] (**1**)	[Zn(L^1)$_2$] (**2**)	[Cu(L^2)$_2$] (**3**)	[Zn(L^2)$_2$] (**4**)
M—O, Å	1.884(2)	1.9878(17)	1.8880(17)	1.971(2), 1.968(2)
M—N_{Im}, Å	1.971(2)	2.0783(18)	2.010(2)	2.058(2), 2.034(2)
M— N_{BTD}, Å	2.071(3)	2.5104(19)		2.425(2)
M—O_{hfac}, Å	1.979(2), 2.244(2)			
trans-angles,°	155.44(9)- 162.14(9)	158.93(7) –169.12(10)	180.00	155.434(85)– 162.141(94)
cis-angles,,°	75.95(9)-117.20(9)	74.46(7) –111.13(10)	89.57(8)- 90.43(8)	75.953(93) – 117.204(82)
π-π, Å	3.552; 3.564	3.536	3.632	3.521; 3.725

In the crystal packing, the complexes form chains along the *b*-axis, connected by π-π stacking interactions (Fig. 5, Table 5). The benzothiadiazole moieties establish intermolecular π-π stacking interactions (see also Figs. S9-S10).

Complexes **3** and **4** crystallize in the monoclinic $P2_1/c$ space group. The crystal structures are quite similar, consisting of a central metal atom and two deprotonated ligands L^2. The ligand displays *O*,*N*-bidentate or *O*,*N*,*N*-tridentate coordination modes, respectively. In the complex **3** the copper ion has a square-planar coordination geometry, with $\tau_4 = 0$ [45] thanks to the N_2O_2 coordinating motif

(Fig. 6). The values of the *trans*-angles are 180.00 °, while the *cis*-angles deviate from 90 ° less than 0.44 °. The bond length distances vary from 1.888 to 2.010 Å (Table 5). In the crystal, π-π stacking interactions (3.632 Å) between benzothiadiazole rings of adjacent molecules are observed (Fig. 6 and Fig. S11).

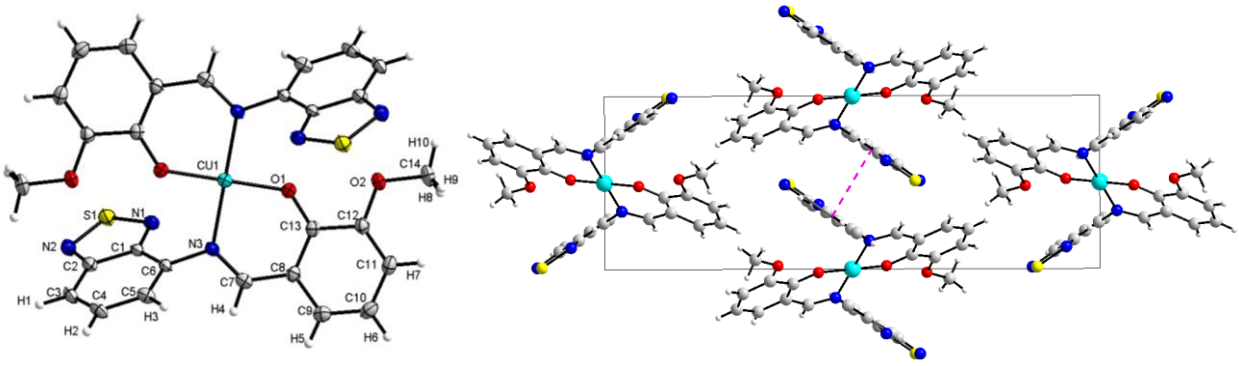

Fig. 6. ORTEP diagram of the molecular structure of **3** showing the atom numbering (left). View of a fragment of the crystal packing of **3** down the crystallographic *a* axis (right).

Unlike **2**, the zinc(II) ion is five-coordinated in compound **4**. The N_3O_2 motif is best described as a slightly distorted square pyramid, as confirmed by the Addison parameter τ_5 = 0.112 [38]. In the equatorial plane, the Zn-N/O bond lengths vary in the range 1.968(2) to 2.058(2) Å, while the axial Zn-N_{BTD} bond distance is 2.425(2) Å. The corresponding *cis*- and *trans*-angles are 75.953(93) – 117.204(82) ° and 155.434(85) – 162.141(94) °, respectively. The zinc atom is displaced from the N_2O_2 plane by 0.349 Å. Molecules of complexes are connected by π-π stacking interactions leading to supramolecular chains running parallel to the *b* axis (Fig. 7). The benzothiadiazole rings take part in the π-π stacking interactions and the Zn···N_{BTD} contacts. Two types of π-π intermolecular interactions are observed: I – 3.521 Å and II – 3.725 Å. The type I involves the non-coordinated benzothiadiazole parts, with the contact Zn1…N4 of 2.973(3) Å and type II involves the coordinated benzothiadiazole units, with the Zn1–N1 bond lengths of 2.425(2) Å (see also Figs. S12-S13).

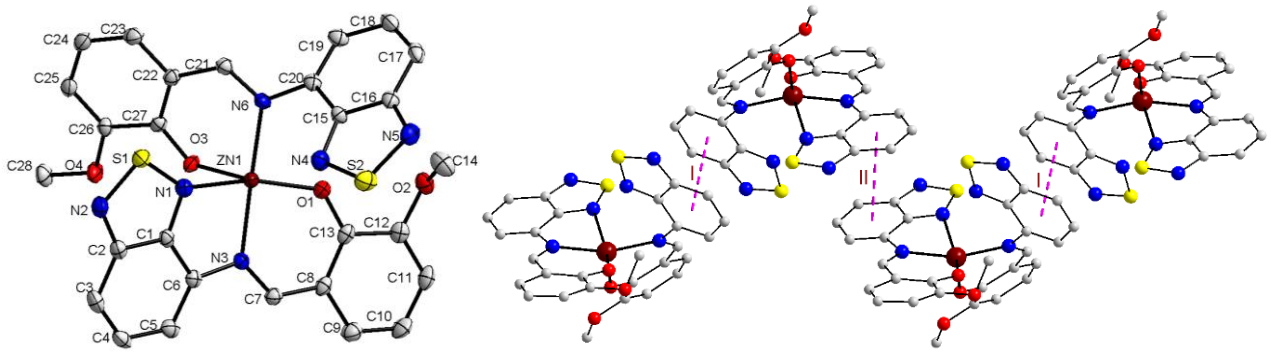

Fig. 7. ORTEP diagram of the molecular structure of complex **4** (left). Fragment of the crystal structures with π-π stacking interactions highlighted (dotted) (right).

3.4. Photophysical properties

The UV-Vis absorption spectra of the Schiff-base ligands were recorded at room temperature in methylene chloride (Fig. 8). The spectra show intense bands in the region 260 – 325 nm and 335 – 435 nm, which can be assigned to n-π* and π-π* transitions. In the case of HL^1 the first band is a combination of two peaks appearing at λ_{max} = 290 nm (34483 cm^{-1}) with ε = 12364 M^{-1} cm^{-1} and at 310 nm (32258 cm^{-1}) with ε = 13857 M^{-1} cm^{-1}; the second band with ε = 11621 M^{-1} cm^{-1} appears at 380 nm (26316 cm^{-1}). The spectrum of HL^2 presents, similarly, two bands at 305 nm (32787 cm^{-1}) and 375 nm (26595 cm^{-1}) with molar absorption coefficients of 10792 and 10792 M^{-1} cm^{-1}, respectively.

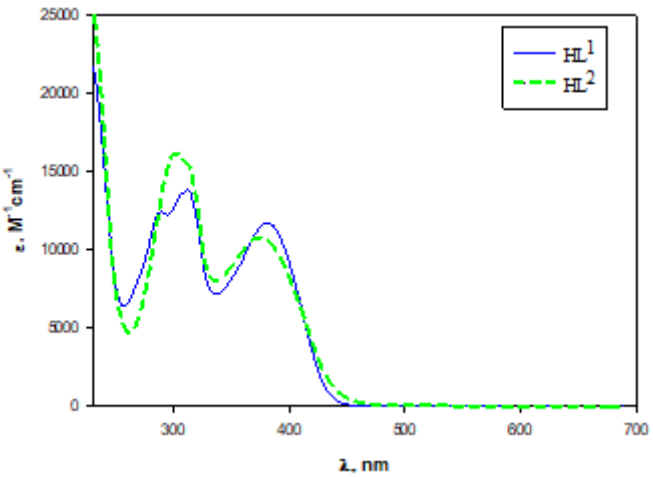

Fig. 8. UV-Vis spectra of HL^1 and HL^2 in methylene chloride (c = 0.05 mM) .

In order to have an insight on the nature of the electronic transitions involved in the absorption bands, we have performed TD-DFT calculations on the ligands with different conformations (see computational details). The experimental spectrum of HL^1 in methylene chloride along with the calculated transitions for *A*- and *B*-conformers are plotted in Fig. 9. The experimental spectrum seems to contain contributions of both conformers, although those corresponding to the *B*-conformer appear to be predominant, especially when considering the low energy band. As pointed out above, the energy difference between the two conformers is relatively weak, therefore it is very likely they are in equilibrium in solution. Taken note of this, the calculated spectrum and electron density difference (EDD) plots, corresponding to the main transitions from the ground state to the excited states, of the *B*-conformer are detailed (Figs. 9 and 10). The first band is a combination of two transitions, i.e. S_1 (absorption at 390 nm, f = 0.269) and S_2 (344 nm, f = 0.069), which correspond to HOMO→LUMO (98%) and HOMO–1→LUMO (95%), respectively. In both cases the EDD show that this band can be described as a phenol to BTD charge transfer. The second band corresponds to a first peak (S_3

state at 317 nm, f = 0.142) plus a second peak which is a combination of S_5 (286 nm, f = 0.093) and S_6 (274 nm, f = 0.137).

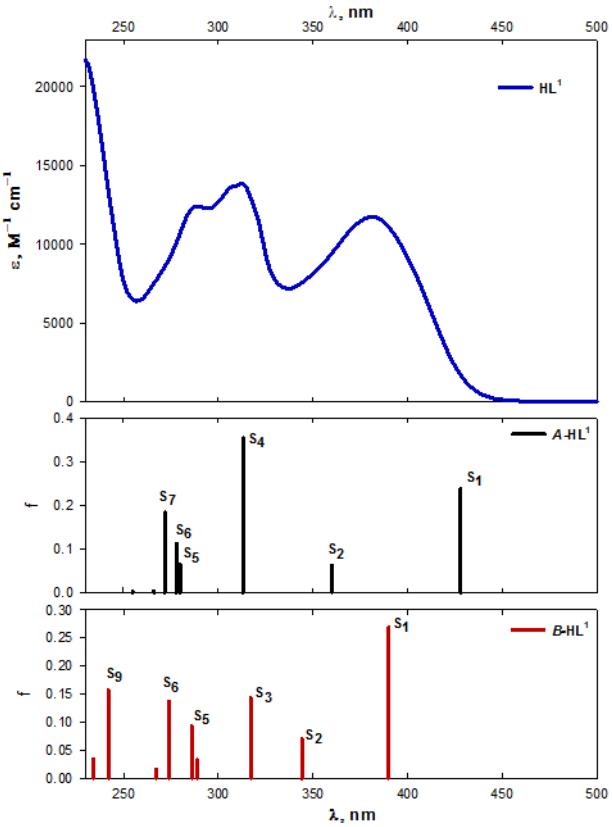

Fig. 9. Experimental absorption spectrum in methylene chloride (top, blue) and calculated oscillator strengths of the *A*- (middle, black) and *B*-conformers (bottom, red) of HL^1.

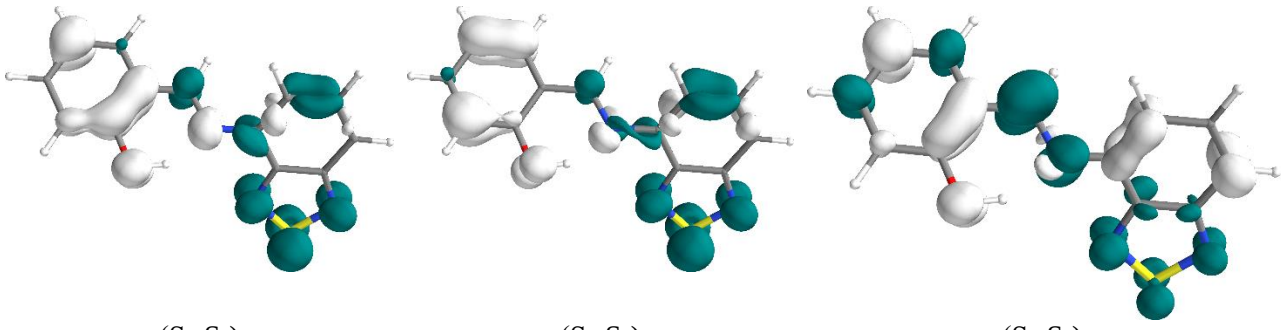

ρ(S_1-S_0) ρ(S_2-S_0) ρ(S_3-S_0)

Fig. 10. Density difference plots between the excited states and the ground state for the *B*-conformer of HL^1 (the excited electron and the hole regions are indicated by respectively blue and white surfaces).

UV-Vis spectra of the zinc(II) complexes **2** and **4** in DMSO at room temperature are presented in Fig. 11. The spectra do not change over a period of four hours, indicating their stability in this solvent. A new band, compared to the spectrum of HL^1 (Fig. 9), at 450 nm (22222 cm^{-1}) and ε = 8814 M^{-1} cm^{-1} for complex **2** and at 460 nm (21739 cm^{-1}) and ε = 6993 M^{-1} cm^{-1} for **4** is observed, probably due to a reduced HOMO–LUMO gap as a consequence of the deprotonation of the Schiff-base molecules.

We have also performed TD-DFT calculations on complexes **2** and **4**. The calculated oscillator strengths are reported in subplots in Fig. 11. To illustrate the electron transfer upon excitation, the EDD plots between the excited state and the ground state are displayed in Fig. 12.

For complex **2**, the first absorption band around 450 nm is mainly due to the third singlet state. The first two singlet excited states present much weaker oscillator strengths (see Table S33). This band can be described as an intra-ligand π-π* transitions from the phenol to the benzothiadiazole moiety with a very small donating contribution of Zn, as shown by the ρS_3-ρS_0 EDD (490 nm, f = 0.205, Fig. 12). There is a strong similarity with the ρS_1-ρS_0 EDD transition in *B*-HL^1 (see Table 6), but also with the ρS_1-ρS_0 EDD transition in L^1 (see Fig. 10 and Table S18), the latter arising at much lower energy because of the drastic decrease of the HOMO-LUMO gap in the anionic deprotonated ligand. Since in **2** the negative charge of the ligand is compensated by the positive one of the metal centre, the bathochromic shift in the UV-vis spectrum of **2** (450 nm and 380 nm) when compared to *B*-HL^1 (Fig. 8) is due to a smaller HOMO-LUMO gap mainly resulting from the higher level of the HOMO in the former.

Concerning the nature of the first absorption band of complex **4**, the results show a strong similarity with the complex **2**. However the absorption corresponds to a combination of the third and fourth excited state (548 nm, f = 0.069 and 516 nm, f = 0.092, see full Table S37) were the excitations are located on only one ligand each time. As in the case of complex **2**, these transitions are intra-ligand π-π* transitions equivalent to the ρS_1-ρS_0 EDD in *B*-HL^2 (see the Fig. S36.) with a small donating contribution of Zn (Fig. 12).

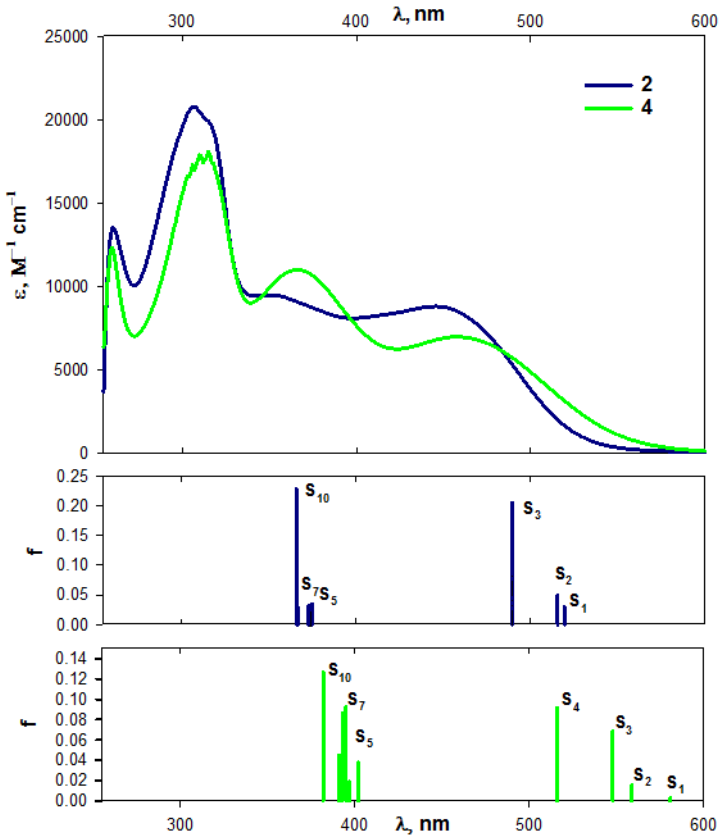

Fig. 11. Experimental absorption spectra in DMSO (c = 0.2 mM) (top, complex **2** blue line, complex **4** green line) and calculated oscillator strengths of the vertical transitions of the complex **2** (middle) and **4** (bottom).

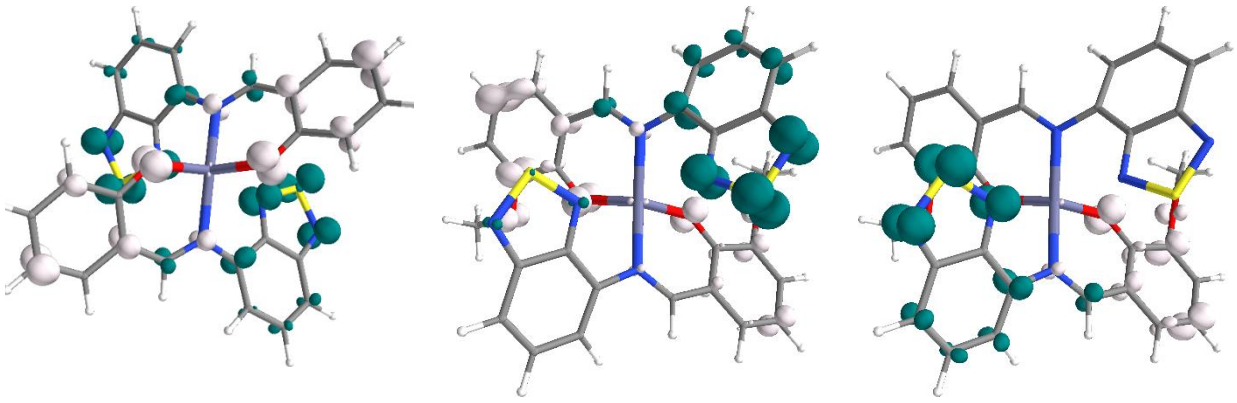

a) ρ(S_3-S_0) b) ρ(S_3-S_0) c) ρ(S_4-S_0)

Fig. 12. Density difference plots between the excited states and the ground state a) **2** and b-c) for complex **4** (the excited electron and the hole regions are indicated by respectively blue and white surfaces).

3.5. Magnetic properties of copper(II) complexes

The magnetic properties of **1** and **3** in the form of $\chi_M T$ *versus* T plot [χ_M is the magnetic susceptibility per copper(II) ion] are shown in Fig. 13. The magnetic properties of both compounds are very similar. At room temperature, the values of $\chi_M T$ are 0.401 (**1**) and 0.409 cm^3 mol^{-1} K (**3**). They correspond,

as expected from the analysis of the crystal structures, to magnetically isolated spin doublets. Upon cooling, these values remain constant until 50 (**1**) and 40 (**3**) K and they further decrease slightly to 0.385 (**1**) and 0.397 cm^3 mol^{-1} K (**3**). The shape of these plots is typical of the occurrence of very weak antiferromagnetic interactions between spin doublets.

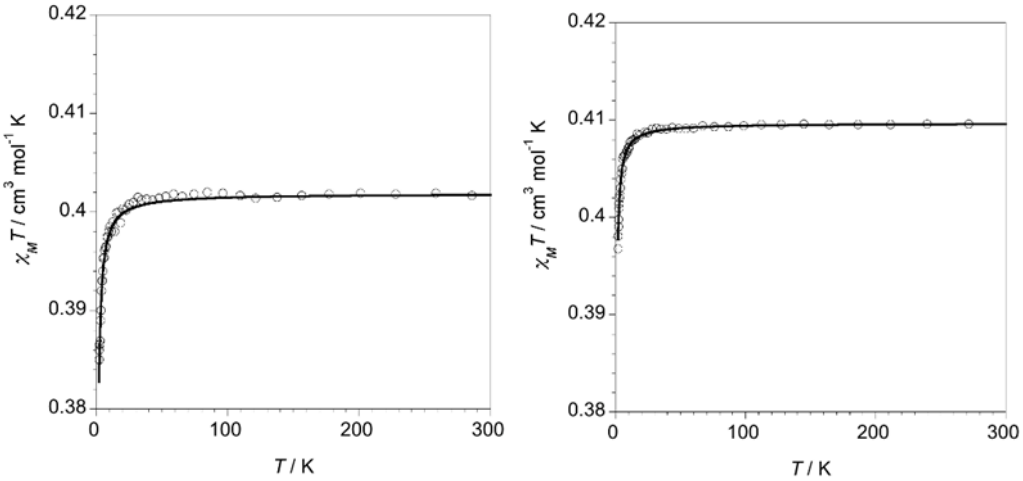

Fig. 13. Thermal dependence of $\chi_M T$ for **1** (left) and **3** (right): (o) experimental; (—) best-fit curve through eq (1).

The analysis of the magnetic data of **1** and **3** by the Curie-Weiss law for a spin doublet, made through the following equation:

$$\chi_M T = N\beta^2 g^2/4(T - \theta) \qquad (1)$$

where θ is a Curie-Weiss term that takes into account the intermolecular magnetic interactions, led to the following best-fit parameters: g = 2.07 and θ = – 0.10 K for **1** and g = 2.09 and θ = – 0.06 K for **3**. The weakness of the antiferromagnetic interaction in the two cases is as expected because of the degree of magnetic isolation between the spin doublets in the two crystal structures [the shortest values of the intermolecular Cu···Cu separation are 6.225 (**1**) and 7.286 Å (**3**)].

4. Conclusions

The new Schiff-base derivative HL^1, derived from the condensation of 4-amino-2,1,3-benzothiadiazole and salicylaldehyde, has been synthesized and structurally characterized, following our previous very recent report on the *ortho*-vanillin analogue HL^2. DFT calculations revealed the existence of two close in energy conformers for HL^1 and HL^2, one corresponding to the experimental X-ray structure and the other to the chelating tridentate form. Both anionic *NNO* phenolate ligands L^1 and L^2 have been investigated for the coordination of the zinc(II) and copper(II) metal ions, DFT calculations on L^1 and L^2 strongly suggesting that the N_{BTD} atoms should be much weakly bonded to the metal centres than the O_{Phen} and N_{Im} atoms. In the resulting complexes **1**-**4**, which have been

structurally investigated, the N_{BTD}–M (M = Cu, Zn) bond is indeed much longer or not observed when compared to the O_{Phen}–M and N_{Im}–M bonds. On the other hand, the BTD unit plays an important role in the establishment on intermolecular π-π interactions. The UV-Vis absorption properties of the zinc(II) complexes have been supported by TD-DFT calculations and compared to those of HL^1 and HL^2. Cryomagnetic measurements show for both copper(II) complexes a Curie-Weiss behaviour indicating the occurrence of very weak antiferromagnetic interactions due to the large separation between the metal ions in the crystal structures and the existence of intermolecular π-π stacking interactions. The use of L^1 and L^2 type ligands is only at its beginning since the choice of transition metal or lanthanide ions is very large. Moreover, the attachment of two salicylaldehyde or *ortho*-vanillin fragments on the BTD platform can be envisaged as a means to access binuclear complexes.

Appendix A. Supplementary data

CCDC 2167426 – 2167430 contain the supplementary crystallographic data for the ligand HL^1 and the complexes **1-4**. These data can be obtained free of charge via http://www.ccdc.cam.ac.uk/conts/retrieving.html, or from the Cambridge Crystallographic Data Centre, 12 Union Road, Cambridge CB2 1EZ, UK; fax: (+44) 1223-336-033; or e-mail: deposit@ccdc.cam.ac.uk.

Acknowledgments

This work was supported in France by the Centre National de la Recherche Scientifique (CNRS), the University of Angers, and the French Embassy in Kyiv, Ukraine (grant to N.P.), and in Spain by the Spanish MICINN (Project PID2019-109735GB-I00).

References

[1] B.A.D. Neto, P.H.P.R. Carvalho, J.R. Correa, Acc. Chem. Res. 48 (2015) 1560–1569.

[2] K.R.J. Thomas, J.T. Lin, M. Velusamy, Y.-T. Tao, C.-H. Chuen, Adv. Funct. Mater. 14 (2004) 83–90.

[3] C.T. Chen, Chem. Mater. 16 (2004) 4389–4400.

[4] L.-Y. Lin, Y.-H. Chen, Z.-Y. Huang, H.-W. Lin, S.-H. Chou, F. Lin, C.-W. Chen, Y.-H. Liu, K.-T. Wong, J. Am. Chem. Soc. 133 (2011) 15822–15825.

[5] Y. Geng, F. Pop, C. Yi, N. Avarvari, M. Grätzel, S. Decurtins, S.-X. Liu, New J. Chem. 38 (2014) 3269–3274.

[6] T. Kono, D. Kumaki, J. Nishida, T. Sakanoue, M. Kakita, H. Tada, S. Tokito, Y. Yamashita, Chem. Mater. 19 (2007) 1218–1220.

[7] M. Zhang, H.N. Tsao, W. Pisula, C. Yang, A.K. Mishra, K. Müllen, J. Am. Chem. Soc. 129 (2007) 3472–3473.

[8] Y. Geng, R. Pfattner, A. Campos, J. Hauser, V. Laukhin, J. Puigdollers, J. Veciana, M. Mas-Torrent, C. Rovira, S. Decurtins, S.-X. Liu, Chem. Eur. J. 20 (2014) 7136–7143.

[9] F. Pop, A. Amacher, N. Avarvari, J. Ding, L.M. Lawson Daku, A. Hauser, M. Koch, J. Hauser, S.-X. Liu, S. Decurtins, Chem. Eur. J. 19 (2013) 2504–2514.

[10] F. Pop, S. Seifert, J. Hankache, J. Ding, A. Hauser, N. Avarvari, Org. Biomol. Chem. 13 (2015) 1040–1047.

[11] T.S. Sukhikh, D.S. Ogienko, D.A. Bashirov, S.N. Konchenkoa, Russ. Chem. Bull. 68 (2019) 651–661.

[12] D. Zhao, D. Yue, K. Jiang, Y. Cui, Q. Zhang, Y. Yang, G. Qian, J. Mater. Chem. C 5 (2017) 1607–1613.

[13] W.-Q. Zhang, Q.-Y. Li, J.-Y. Cheng, K. Cheng, X. Yang, Y. Li, X. Zhao, X.-J. Wang, ACS Appl. Mater. Interfaces 9 (2017) 31352–31356.

[14] Q. Cheng, X. Han, Y. Tong, C. Huang, J. Ding, H. Hou, Inorg. Chem. 56 (2017) 1696–1705.

[15] R.J. Marshall, Y. Kalinovskyy, S.L. Griffin, C. Wilson, B.A. Blight, R.S. Forgan, J. Am. Chem. Soc. 139 (2017) 6253–6260.

[16] M. Akhtaruzzaman, M. Tomura, M. B. Zaman, J. Nishida, Y. Yamashita, J. Org. Chem. 67 (2002) 7813–7818.

[17] M. Akhtaruzzaman, M. Tomura, J. Nishida, Y. Yamashita, J. Org. Chem. 69 (2004) 2953–2958.

[18] W.-C. Song, L. Liang, X.-Z. Cui, X.-G. Wang, E.-C. Yang, X.-J. Zhao, CrystEngComm 20 (2018) 668–678.

[19] T. Mocanu, N. Plyuta, T. Cauchy, M. Andruh, N. Avarvari, Chemistry 3 (2021) 269–287.

[20] X. Song, H. Yu, X. Yan, Y. Zhang, Y. Miao, K. Ye, Y. Wang, Dalton Trans. 47 (2018) 6146–6155.

[21] M. Munakata, H. He, T. Kuroda-Sowa, M. Maekawa, Y. Suenaga, J. Chem. Soc., Dalton Trans. (1998) 1499–1502.

[22] T.S. Sukhikh, D.A. Bashirov, D.S. Ogienko, N.V. Kuratieva, P.S. Sherin, M.I. Rakhmanova, E.A. Chulanova, N.P. Gritsan, S.N. Konchenko, A.V. Zibarev, RSC Adv. 6 (2016) 43901–43910.

[23] M. Andruh, Chem. Commun. 47 (2011) 3025–3042.

[24] R.M. Clarke, T. Storr, Dalton Trans. 43 (2014) 9380–9391.

[25] M. Andruh, Dalton Trans. 44 (2015) 16633–16653.

[26] N. Plyuta, S. Petrusenko, V.N. Kokozay, T. Cauchy, F. Lloret, M. Julve, J. Cano, N. Avarvari, Dalton Trans. 51 (2022) 4760–4771.

[27] G.M. Sheldrick, SHELX-97, Program for Crystal Structure Refinement; University of Göttingen: Göttingen, Germany, 1997.

[28] G.M. Sheldrick, SHELXL-97, Program for Crystal Structure Solution; University of Göttingen: Göttingen, Germany, 1997.

[29] L.J. Farrugia, WINGX, A Windows Program for Crystal Structure Analysis, University of Glasgow, UK, 1988.

[30] M.J. Frisch et al., Gaussian 09, Revision D.01, Gaussian Inc., Wallingford CT, 2016.

[31] C. Adamo, V. Barone, J. Chem. Phys. 110 (1999) 6158–6170.

[32] A. Schäfer, H. Horn, R. Ahlrichs, J. Chem. Phys. 97 (1992) 2571–2577.

[33] A. Schäfer, C. Huber, R. Ahlrichs, J. Chem. Phys. 100 (1994) 5829–5835.

[34] F.L. Hirshfeld, Theor. Chem. Acc. 44 (1977) 129–138.

[35] J.P. Ritchie, S.M. Bachrach, J. Comp. Chem. 8 (1987) 499–509.

[36] T. Cauchy, B. Da Mota, quchemreport. A python program for control quality and automatic generation of quantum chemistry results, University of Angers, 2020.

[37] N.M. O'Boyle, A.L. Tenderholt, K.M. Langner, J. Comput. Chem. 29 (2008) 839–84.

[38] A.W. Addison, T.N. Rao, J. Reedijk, J. van Rijn, G.C. Verschoor, J. Chem. Soc., Dalton Trans. (1984) 1349–1356.

[39] R. Khisamov, T. Sukhikh, D. Bashirov, A. Ryadun, S. Konchenko, Molecules 25 (2020) 2428.

[40] T.S. Sukhikh, R.M. Khisamov, D.A. Bashirov, V.Yu. Komarov, M.S. Molokeev, A.A. Ryadun, E. Benassi, S.N. Konchenko, Cryst. Growth Des. 20 (2020) 5796–5807.

[41] X. Han, Q. Cheng, X. Meng, Z. Shao, K. Ma, D. Wei, J. Ding, H. Hou, Chem. Commun. 53 (2017) 10314–10317.

[42] K. Ma, Y. Zhao, X. Han, J. Ding, X. Meng, H. Hou, Cryst. Growth Des. 18 (2018) 7419–7425.

[43] S. Alvarez, P. Alemany, D. Casanova, J. Cirera, M. Llunell, D. Avnir, Coord. Chem. Rev. 249 (2005) 1693–1708.

[44] J. Cirera, E. Ruiz, S. Alvarez, Chem. Eur. J. 12 (2006) 3162–3167.

[45] L. Yang, D.R. Powell, R.P. Houser, Dalton Trans. (2007) 955–964.